Editors' Suggestion | Featured in Physics

Large spontaneous magneto-thermoelectric effect in epitaxial thin films of the topological kagome ferromagnet Fe_3Sn

Shun'ichiro Kurosawa,[1] Tomoya Higo,[1,2,*] Shota Saito,[1] Ryota Uesugi,[2] and Satoru Nakatsuji[1,2,3,4,5,†]

[1]*Department of Physics, The University of Tokyo, Bunkyo-ku, Tokyo 113-0033, Japan*

[2]*Institute for Solid State Physics, The University of Tokyo, Kashiwa, Chiba 277-8581, Japan*

[3]*Institute for Quantum Matter and Department of Physics and Astronomy, Johns Hopkins University, Baltimore, Maryland 21218, USA*

[4]*Trans-Scale Quantum Science Institute, The University of Tokyo, Bunkyo-ku, Tokyo 113-0033, Japan*

[5]*Canadian Institute for Advanced Research, Toronto, M5G 1Z7, Ontario, Canada*

(Received 17 January 2024; accepted 10 April 2024; published 28 May 2024)

Recent intensive studies in metallic kagome systems have revealed various correlated topological and electronic states, leading to their spintronic applications. The kagome ferromagnetic metal Fe_3Sn has been found to host a topological nodal plane near the Fermi energy and exhibits large transverse transport responses. Here we report the fabrication of the epitaxial thin films of Fe_3Sn and the observation of its large anomalous Nernst effect (ANE). Structural and magnetic measurements reveal (0001)-orientated epitaxial growth of kagome $D0_{19}$ Fe_3Sn and the magnetic easy plane along the substrate plane. Moreover, transport measurements confirm the large ANE of 2.4 μV/K at room temperature, comparable to that of the bulk polycrystalline samples. The obtained Fe_3Sn film should be useful for thermoelectric applications, because the binary compound based on inexpensive elements exhibits large spontaneous ANE voltage under an out-of-plane heat current due to the magnetic and electronic states stabilized by the magnetic anisotropy.

DOI: 10.1103/PhysRevMaterials.8.054206

I. INTRODUCTION

The kagome lattice, a two-dimensional network of corner-sharing triangles, has emerged as a fascinating platform to study exotic electronic phases due to the intricate interplay among band topology, electronic correlations, and frustrated magnetism. In particular, metallic kagome systems feature distinct signatures in their electronic structure, such as the topological Dirac and Weyl points, flat bands, and van Hove singularities, leading to fascinating phenomena, including the emergence of correlated topological states, charge-density-wave order, and superconductivity. Extensive studies have revealed a large number of kagome materials, including binary metal T_xSn_y systems (T = Fe, Mn, Co and $x : y = 1 : 1, 3 : 2, 3 : 1$) [1–7], Co shandite $Co_3Sn_2S_2$ [8–11], rare-earth-based ReT'_6Sn_6 systems (Re = Gd, Tm, Tb, Y, and T' = Mn, V) [12–14], and AV_3Sb_5 systems (A = K, Cs, Rb) [15–17], exhibit novel emergent properties and attracted wide-ranging interest from fundamental to applied fields. Among them, Mn_3Sn is the first metallic kagome magnet that has attracted tremendous interest for its nontrivial transport properties and stands out as one of the rare cases where a noncollinear antiferromagnetic (AFM) state is realized due to its geometrical frustration [1]. The antichiral 120-degree ordering stabilizes a magnetic Weyl semimetal state [2] and enables the very exciting observation of anomalous Hall effect (AHE) [1], anomalous Nernst effect (ANE) [18,19], and magneto-optical Kerr and Faraday effects [20,21] in AFM state with vanishingly small magnetization at room temperature. Recent successful electrical switching [22,23] and readout of the chiral antiferromagnetic state through tunneling magnetoresistance [24] have placed the compound as one of the most promising key materials for developing antiferromagnetic spintronics [25].

On the other hand, the Fe–Sn families provide a variety of kagome metals with different dimensionalities of the kagome Fe_3Sn layer, exhibiting interesting phenomena mainly at low temperatures. For example, the kagome ferromagnet (FM) Fe_3Sn_2, composed of the kagome Fe_3Sn layer and the honeycomb Sn_2 layer, shows the emergence of the massive Dirac fermions, the Weyl fermions, the flat bands, and skyrmion spin texture [3,26–29]. An analogous material, FeSn, in which Fe_3Sn and Sn_2 layers have different stacking orders, becomes AFM and also exhibits the coexistence of the bulk and surface Dirac fermions, as well as the flat bands [4,30,31]. Furthermore, studies of Fe–Sn films have shown that even the short-range ordering of the kagome lattice fragments can contribute to the realization of the large AHE [32] and transverse magneto-thermoelectric effect induced by the Berry curvature [33].

Recent theoretical and experimental studies on bulk polycrystalline samples have revealed that the kagome FM Fe_3Sn, isostructural to the chiral AFM Mn_3Sn, hosts a novel topological electronic structure, nodal plane near the Fermi energy [5]. The nodal plane consists of two nearly flat bands that are closely facing each other in two dimensions. The tiny energy gap and flat band dispersion enhance both the Berry curvature and the density of states (DOS), leading to the large

*Corresponding author: tomoyahigo@g.ecc.u-tokyo.ac.jp

†Corresponding author: satoru@phys.s.u-tokyo.ac.jp

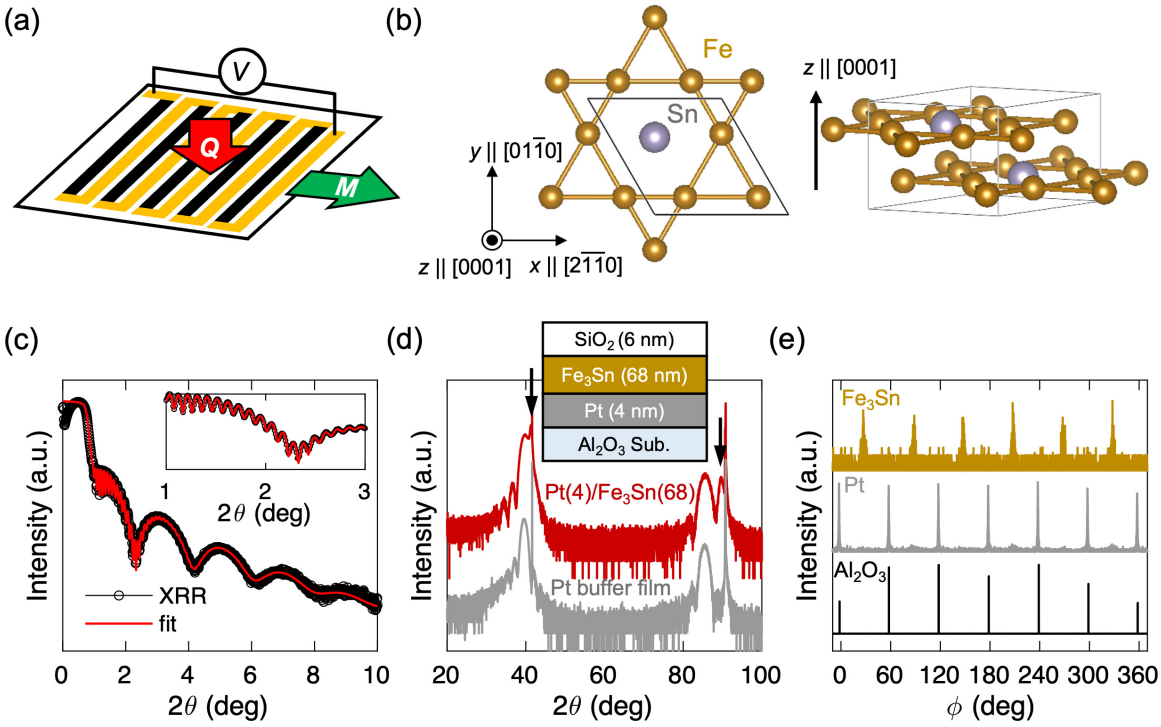

FIG. 1. (a) Schematic illustration of a thermoelectric device using ANE. Black lines are the magnetic metals, and yellow lines are the electrodes. (b) Crystal structure of the kagome ferromagnet Fe_3Sn. The yellow and gray spheres represent the Fe and Sn atoms, respectively. Figures of crystal structure are generated with VESTA [77]. (c) X-ray reflectivity results of the Al_2O_3/Pt/Fe_3Sn/SiO_2 film. The red curve shows the fitting result. Inset: Expanded plot between 1 and 3°. (d) X-ray diffraction patterns of the Al_2O_3/Pt/Fe_3Sn/SiO_2 film (red line) and the Al_2O_3/Pt/SiO_2 film (gray line). The arrows indicate the peaks of Fe_3Sn (0002) and (0004). Inset: Film structure of Fe_3Sn and Pt bilayer on the Al_2O_3 (0001) substrate. The number in the bracket of the sample label is the thickness of each layer. (e) In-plane scan of the Fe_3Sn {1$\bar{2}$12} (dark yellow line), Pt {$\bar{1}$11} (gray line), and Al_2O_3 {$\bar{2}$116} (black line) reflections. Measurements are all made at room temperature.

ANE S_{yx} and transverse thermoelectric conductivity α_{yx}. In fact, the large $|S_{yx}|$ of 2.9 μV/K and $|\alpha_{yx}|$ of 2.3 A/Km were observed in bulk Fe_3Sn polycrystalline samples at room temperature [5]. Fe_3Sn has a high Curie temperature above 700 K and exhibits a large magnetization of 6.8 μ_B/f.u. aligned within the kagome layer due to the easy-plane magnetic anisotropy [34–37]. In this ferromagnetic phase, the magneto-thermoelectric response increases linearly with temperature at a rate of ∼0.8 μV/K for every 100 K up to 400 K.

ANE provides the measure of DOS associated with the Berry curvature at the Fermi energy and thus can be strongly enhanced in topological magnets [9,18,19,25,38–45]. The recent discovery of the enhanced ANE in topological magnets has fostered the research and development for applying ANE to thermoelectric technologies. In comparison with the Seebeck effect (SE), ANE generates an electromotive force orthogonal to the temperature gradient and magnetization, allowing a lateral device structure [Fig. 1(a)], whereas SE requires a three-dimensional π-shaped device structure. Thus, compared to the SE-based technology, ANE enables much lower costs and simpler fabrication processes for large-area and flexible thermoelectric devices, such as energy harvesters and heat-flux sensors [46,47].

Recent advances in sample preparation techniques have enabled the fabrication of bulk single crystals [37,48,49] and epitaxial thin films of Fe_3Sn [50]. No anisotropic thermoelectric properties, however, have been clarified to date for Fe_3Sn. In addition, none of the magneto-thermoelectric properties have been investigated in any thin-film form of Fe_3Sn, while the magneto-thermoelectric properties in thin-film samples are essential for device applications. Here, we have fabricated epitaxial thin films of the nodal plane FM Fe_3Sn and investigated their magnetic and magneto-thermoelectric properties. The large easy-plane magnetic anisotropy and giant Hall conductivity exceeding previously reported values on bulk crystals confirm the successful fabrication of high-quality Fe_3Sn epitaxial films. We have also obtained a large ANE higher than that of bulk polycrystalline samples and confirmed that this effect shows large spontaneous power output in the configuration for the perpendicular heat current required for fabricating thermoelectric devices [46,47,51–53]. These results pave the way for potential device applications such as ANE-based energy harvesters and heat-flux sensors.

II. METHODS

Fe_3Sn has a hexagonal $D0_{19}$ structure with a space group of $P6_3/mmc$ ($a = 5.46$ Å, $c = 4.35$ Å) [5,37,48] consisting of Fe-based kagome lattice stacked along [0001] as shown in Fig. 1(b). Hereafter, we fix the orthogonal frame x, y, and z to the crystalline directions [2$\bar{1}\bar{1}$0], [01$\bar{1}$0], and [0001], respectively [Fig. 1(b)]. We employ an rf sputtering method to fabricate Fe_3Sn epitaxial films on an Al_2O_3 (0001) substrate with a Pt buffer layer [50]. The base pressure of the rf sputtering chamber is $< 3 \times 10^{-4}$ Pa. First, the Pt layer (4 nm) is deposited at 550 °C on the Al_2O_3 substrate, followed by

the Fe_3Sn layer deposited at 350 °C. After fabrication of each layer, films are annealed for 30 minutes while maintaining each deposition temperature. A SiO_2 capping layer is finally fabricated at around room temperature to prevent oxidation. The mosaic target, which consists of a Fe_3Sn alloy target and additional Sn tips, is used to control the composition of the Fe_3Sn layer, which is confirmed to be $Fe_{3.1}Sn_{0.9}$ by x-ray fluorescence measurements. The structural analysis is performed by x-ray diffraction (XRD) measurements, and the thickness of the films is estimated by the x-ray reflectivity (XRR) measurement using an automated multipurpose x-ray diffractometer (Smart Lab, Rigaku) with Cu $K\alpha 1$ source ($\lambda = 1.54$ Å). The magnetic properties are measured using a superconducting quantum interference device in a commercial magnetic property measurement system (MPMS3, Quantum Design). The electrical and thermal transport properties are measured by a commercial physical property measurement system (PPMS, Quantum Design) with thermal transport options and by a homemade measurement system using a variable-temperature insert with a superconducting magnet (Teslatron PT, Oxford Instruments).

III. RESULTS AND DISCUSSION

A. Structural characterization

Figure 1(c) shows the result of XRR measurements for a Pt/Fe_3Sn/SiO_2 film on Al_2O_3 substrate. Fitting the XRR spectrum shown in Fig. 1(c) reveals that the thicknesses of the Fe_3Sn layer (t_{Fe_3Sn}), the Pt layer (t_{Pt}), and the SiO_2 layer (t_{SiO_2}) are 68 nm, 4 nm, and 6 nm, respectively [Fig. 1(d) inset]. In addition, the root mean square (RMS) roughness of the Fe_3Sn layer is estimated to be ∼0.9 nm. The 2θ–θ scans in XRD measurements confirm the peaks at around 40° and 90°, respectively corresponding to the (0002) and (0004) peaks of Fe_3Sn and at around 39° and 85° corresponding to the (111) and (222) peaks of Pt in the Al_2O_3/Pt/Fe_3Sn/SiO_2 film (red line) and Al_2O_3/Pt/SiO_2 film (gray line), as shown in Fig. 1(d). Moreover, the ϕ-scan measurements reveal the sixfold symmetry for the $\{1\bar{2}12\}$ peaks of Fe_3Sn (dark yellow line), the $\{\bar{1}11\}$ peaks of Pt (gray line), and the $\{\bar{2}116\}$ peaks of Al_2O_3 (black line) [Fig. 1(e)]. The observed sixfold symmetric peaks of the Pt layer indicate the presence of a twinning structure of (111)-oriented Pt grains rotating 180° around the Pt [111] pole relative to the other grains, consistent with previous reports [54–56]. (See Fig. S1 in the Supplemental Material [57].) Moreover, the Fe_3Sn peaks are shifted by 30° with respect to the Pt and Al_2O_3 peaks. These results indicate the epitaxial growth of the Fe_3Sn layer with the crystallographic relation Al_2O_3 (0001) $\langle 2\bar{1}\bar{1}0\rangle$|| Pt (111) $\langle \bar{1}2\bar{1}\rangle$|| Fe_3Sn (0001) $\langle 01\bar{1}0\rangle$.

B. Magnetic properties

Figure 2(a) shows the magnetic field dependence of the magnetization of the Fe_3Sn epitaxial film at 300 K. The field dependence and the saturated magnetization $M_s = 7.6\ \mu_B$/f.u. ($\mu_0 M_s = 1.6$ T) are comparable to that obtained in the bulk samples [5,34,35,37]. In addition, the easy-plane magnetic anisotropy can be confirmed by comparing the magnetization parallel and perpendicular to the kagome plane. The magnetic field

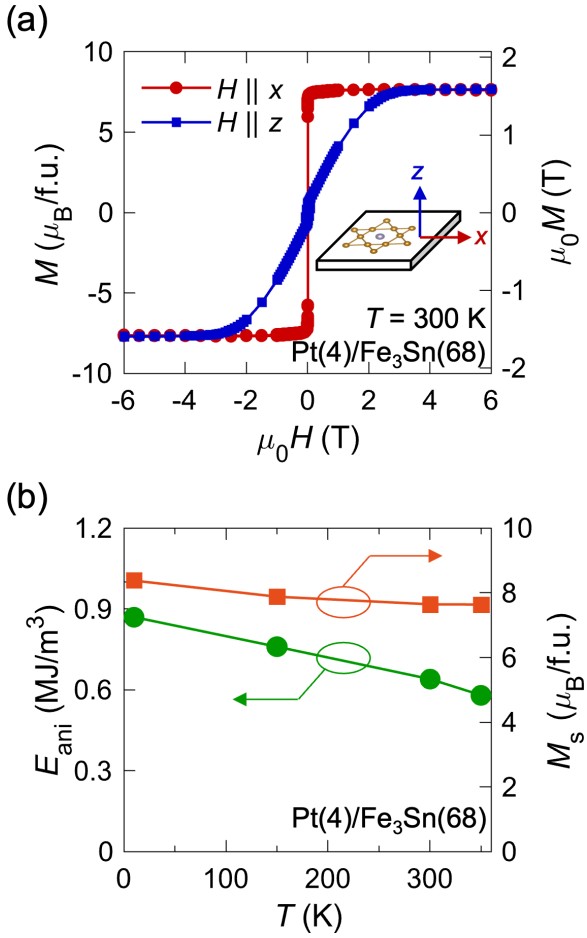

FIG. 2. (a) Field dependence of the magnetization along $[2\bar{1}\bar{1}0]$ (|| x) (red circle) and [0001] (|| z) (blue square) at room temperature of the Al_2O_3/Pt/Fe_3Sn/SiO_2 film. Inset: Schematic illustration of the magnetization measurement along $[2\bar{1}\bar{1}0]$ (|| x) (red circle) and [0001] (|| z) (blue square) configuration. (b) Temperature dependence of the magnetocrystalline anisotropy (green circle) and the saturated magnetization (orange square).

required to saturate the magnetization in the perpendicular direction is $\mu_0 H_s = 2.6$ T. Even after subtracting the contribution of the demagnetizing field ($\mu_0 M_s = 1.6$ T), the magnetic anisotropy field of ∼1 T, which corresponds to the magnetocrystalline anisotropy of $E_{ani} = \mu_0 M_s (H_s - M_s)/2 = 0.64\,\mathrm{MJ/m^3}$, still aligns the magnetization parallel to the kagome layer. In addition, E_{ani} gradually increases with decreasing temperature and reaches 0.87 $\mathrm{MJ/m^3}$ at 10 K [Fig. 2(b)]. These E_{ani} are ∼10 times larger than the previously reported value for the ultrathin epitaxial films [50] and are comparable to that confirmed in the bulk single crystals [37] ($E_{ani} = 0.97$ (1.27) $\mathrm{MJ/m^3}$ at 300 (2) K). These magnetic properties as well as the XRD measurements indicate the high-quality crystallinity of $D0_{19}$ Fe_3Sn film.

C. Electrical transport properties

We now move on to the transport properties of the Fe_3Sn epitaxial film. Figure 3(a) shows the magnetic field dependence of AHE at room temperature under the field along the z axis. The observed Hall resistivity ρ_{yx} of the

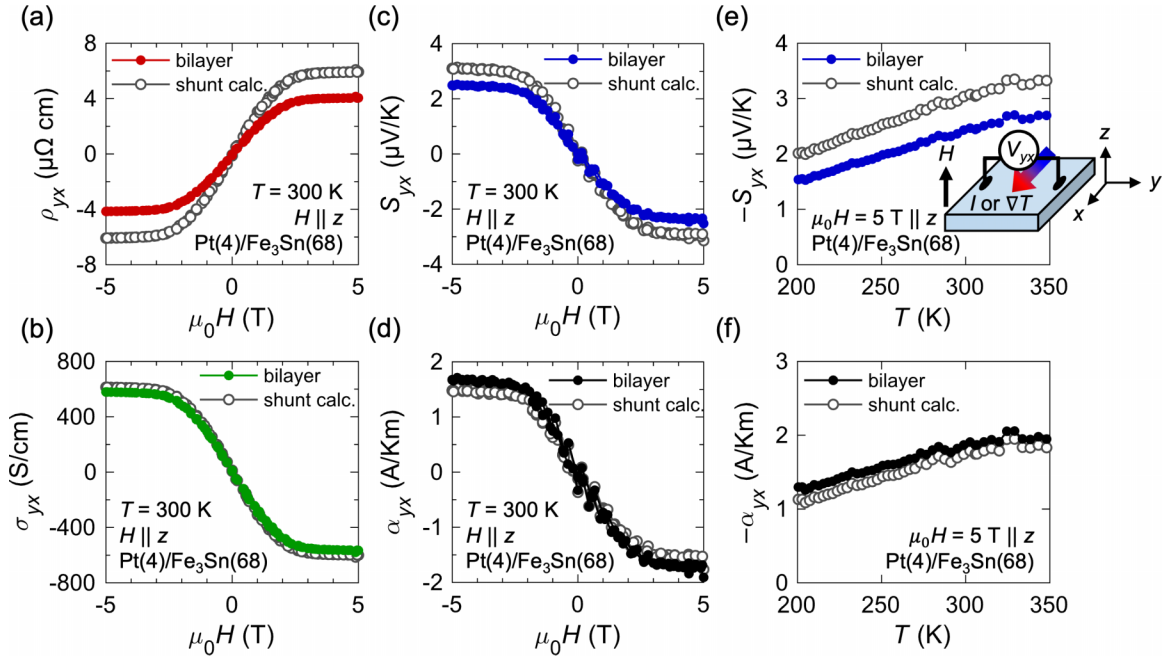

FIG. 3. Field dependence of (a) the Hall resistivity, (b) the Hall conductivity, (c) ANE, and (d) the transverse thermoelectric conductivity α_{yx} of the Al_2O_3/Pt/Fe_3Sn/SiO_2 film under the out-of-plane field H ($\parallel [0001] \parallel z$) and in-plane electric current I or temperature gradient ∇T ($|| [2\bar{1}\bar{1}0] || x$) configuration at room temperature. (e, f) Temperature dependence of (e) ANE and (f) α_{yx} from 200 to 350 K under $\mu_0 H = 5$ T. The colored curves in (a)–(f) are the results of the Pt/Fe_3Sn bilayer. On the other hand, the gray curves with open circles represent corrected data considering the shunting effect. Inset in (e): Schematic illustration of the setup for the AHE (ANE) measurements under the out-of-plane field H and the in-plane electric current I (temperature gradient ∇T).

Al_2O_3/Pt/Fe_3Sn/SiO_2 film (red circles) shows the saturation at 2.5 T with the saturated Hall resistivity of 4.1 μΩ cm. Here we use the thickness of the Pt/Fe_3Sn bilayer ($t = t_{Fe_3Sn} + t_{Pt} =$ 72 nm) for the calculation. However, in a bilayer consisting of a ferromagnetic metal layer and a nonmagnetic metal layer, the Hall voltage signal generated in the ferromagnetic layer V_{Fe_3Sn} is suppressed by the electrical conduction in the nonmagnetic layer, namely, the shunting effect [69,70]. This effect can be described in the following equation:

$$V_{Fe_3Sn} = V_{yx}\left(1 + \frac{\rho_{Fe_3Sn}}{\rho_{Pt}}\frac{t_{Pt}}{t_{Fe_3Sn}}\right) \equiv V_{yx}\zeta. \quad (1)$$

Here, V_{yx} denotes the experimentally observed Hall voltage, ρ_{Fe_3Sn} the resistivity of the Fe_3Sn layer, ρ_{Pt} the resistivity of the Pt layer, and ζ the factor due to the shunting effect. Moreover, ignoring the interface resistance, the current flowing in the Fe_3Sn layer I_{Fe_3Sn} is diverted from the applied read current I and is described as follows:

$$I_{Fe_3Sn} = I/\zeta. \quad (2)$$

Therefore, the calculated Hall resistivity in the Fe_3Sn layer ρ_{yx}^{calc} can be estimated from the equation

$$\rho_{yx}^{calc} = \frac{V_{Fe_3Sn}}{I_{Fe_3Sn}} t_{Fe_3Sn} = \frac{V_{yx}}{I} t \zeta^2 \frac{t_{Fe_3Sn}}{t} = \rho_{yx}\zeta^2 \frac{t_{Fe_3Sn}}{t}. \quad (3)$$

To evaluate ζ, we additionally prepared the Pt single-layer sample with the same fabrication process as that used for the Pt layer in the Al_2O_3/Pt/Fe_3Sn/SiO_2 film and estimated the longitudinal resistivity of the Pt layer to be $\rho_{Pt} = 24$ μΩ cm. This allows us to estimate the resistivity of the Fe_3Sn layer and the shunt factor ζ to be $\rho_{Fe_3Sn} = (t/\rho_{xx} - t_{Pt}/\rho_{Pt})^{-1} t_{Fe_3Sn} =$ 100 μΩ cm and $\zeta = 1.25$, respectively. Here ρ_{xx} denotes the experimentally obtained longitudinal resistivity ($\rho_{xx} =$ 85 μΩ cm), which corresponds to the resistivity of the metallic bilayer. The gray open circles in Fig. 3(a) present the calculated Hall resistivity in the Fe_3Sn layer ρ_{yx}^{calc}, taking into account the shunting effect, and the saturated ρ_{yx}^{calc} is estimated to be 6.0 μΩ cm. Moreover, we estimate the Hall conductivity of the bilayer $\sigma_{yx} \approx -\rho_{yx}/\rho_{xx}^2$ (green circles) and the calculated Hall conductivity in the Fe_3Sn layer $\sigma_{yx}^{calc} \approx -\rho_{yx}^{calc}/\rho_{Fe_3Sn}^2$ (gray open circles), as shown in Fig. 3(b). Their saturated values are $|\sigma_{yx}| = 570$ S/cm and $|\sigma_{yx}^{calc}| =$ 605 S/cm, much larger than both bulk polycrystalline samples [5] (490 S/cm) and single-crystal samples [48,49] (485 S/cm and 500 S/cm), indicating the successful fabrication of the high-crystallinity epitaxial films of Fe_3Sn.

D. Magneto-thermoelectric properties

The intrinsic contribution of AHE originates from the momentum-space Berry curvature in the occupied bands below the Fermi energy E_F, as described by the equation $\sigma_{yx} = \epsilon_{xyz}(e^2/\hbar)\int_{\boldsymbol{k}} (2\pi)^{-3} \sum_n [\Omega_{n,z}(\boldsymbol{k}) f(\varepsilon_{n,\boldsymbol{k}})] d\boldsymbol{k}$. Here ϵ_{xyz}, e, $\hbar$, π, $\Omega_{n,z}$, f and $\varepsilon_{n,\boldsymbol{k}}$ denote the antisymmetric tensors, the elementary charge, the reduced Planck constant, the circular constant, the Berry curvature for the z direction, the Fermi-Dirac distribution function, and the band energy with band index n and wave vector $\boldsymbol{k}$, respectively. On the other hand, the transverse

magneto-thermoelectric conductivity given by the equation $\alpha_{yx} = (k_B/e)\int \epsilon_{xyz} \sum_{n,\boldsymbol{k}} [\Omega_{n,z}(\boldsymbol{k})\delta(\varepsilon - \varepsilon_{n,\boldsymbol{k}})]s(\varepsilon, T)\mathrm{d}\varepsilon$, where $s(\varepsilon, T)$ is the entropy density, is related to the Berry curvature around E_F, which is found particularly enhanced in the topological magnetic materials [9,18,19,25,38–45,71–73]. For the highly crystallized Fe_3Sn films, giant transverse responses are also expected in ANE $S_{yx} = \rho_{yy}(\alpha_{yx} - \sigma_{yx}S_{xx})$, which consists of contributions from the Hall conductivity and the transverse magneto-thermoelectric conductivity. Here S_{xx} denotes the Seebeck coefficient. Figure 3(c) shows the magnetic field dependence of ANE at 300 K under the out-of-plane magnetic field ($H \parallel z$) and the in-plane temperature gradient ($\nabla T \,||\, x$) [Fig. 3(e) inset]. Experimentally, S_{yx} can be calculated by $S_{yx} = V_{yx}/(d\nabla T)$, where V_{yx} is the transverse voltage and d is the length between transverse voltage terminals. The experimentally obtained S_{yx} of the Al_2O_3/Pt/Fe_3Sn/SiO_2 film (blue circles) shows the large saturated signal of $|S_{yx}| = 2.4\ \mu V/K$. Unlike in the case of AHE that requires the electric current, the shunting effect does not affect ∇T because the heat flow in films is determined by the substrate [39]. Therefore, the shunting effect only needs to be considered for the transverse direction ($\parallel y$), where the electromotive force is generated. The calculated ANE in the Fe_3Sn layer can be obtained by using the equation $S_{yx}^{calc} = S_{yx}\zeta$. As presented by the gray open circles in Fig. 3(c), we confirm $|S_{yx}^{calc}| = 3.0\,\mu V/K$, comparable to or even larger than that obtained in the Fe_3Sn bulk polycrystals ($|S_{yx}| = 2.9\,\mu V/K$) [5]. Our measurement finds the Seebeck coefficient to be $S_{xx} = -20\,\mu V/K$ ($S_{xx}^{calc} = -25\,\mu V/K$). Using these values, the transverse thermoelectric conductivity $|\alpha_{yx}| = |\sigma_{xx}S_{yx} + \sigma_{yx}S_{xx}|$ for the Pt/Fe_3Sn bilayer and $|\alpha_{yx}^{calc}| = |\sigma_{xx}^{calc}S_{yx}^{calc} + \sigma_{yx}^{calc}S_{xx}^{calc}|$ for the Fe_3Sn single layer are estimated to be 1.7 A/Km and 1.5 A/Km, respectively [Fig. 3(d)]. Here, the electric conductivities σ_{xx} and σ_{xx}^{calc} are calculated by the equations $\sigma_{xx} = 1/\rho_{xx}$ and $\sigma_{xx}^{calc} = 1/\rho_{Fe_3Sn}$. Interestingly, in contrast to ρ_{yx}, σ_{yx}, and S_{yx}, the transverse thermoelectric conductivity is smaller than that confirmed in the Fe_3Sn bulk polycrystalline samples [5] ($|\alpha_{yx}| = 2.3$ A/Km) but far larger than those for the conventional FMs [38]. The large α_{yx} suggests that the observed ANE is enhanced by the large Berry curvature due to the nodal plane near the Fermi level. Figures 3(e) and 3(f) show the temperature dependence of S_{yx} and α_{yx} between 200 and 350 K under 5 T. Both $|S_{yx}|$ and $|\alpha_{yx}|$ ($|S_{yx}^{calc}|$ and $|\alpha_{yx}^{calc}|$) increase monotonically and reach 2.7 μV/K and 2.0 A/Km (3.3 μV/K and 1.8 A/Km) at 350 K for the Pt/Fe_3Sn bilayer (Fe_3Sn single layer), respectively. For future work, it is important to investigate the thermoelectric performance up to 600 K, where the thermoelectric devices can be applied to energy harvesters at the near-room-temperature region where the waste heat is the most available.

Next, we show ANE under the out-of-plane ∇T [Fig. 4(a)], where the voltage signal V_{xz} for the longer in-plane direction ($l = 5.1$ mm) was measured under the magnetic field applied in the shorter in-plane direction ($w = 2.0$ mm). Figure 4(b) shows the field dependence of V_{xz} for the Al_2O_3(430 μm)/Pt(4 nm)/Fe_3Sn(68 nm)/SiO_2(6 nm) film at 300 K. Here, the heater power is set to produce the temperature difference of 1.5 K between thermocouples located at the top and bottom of the

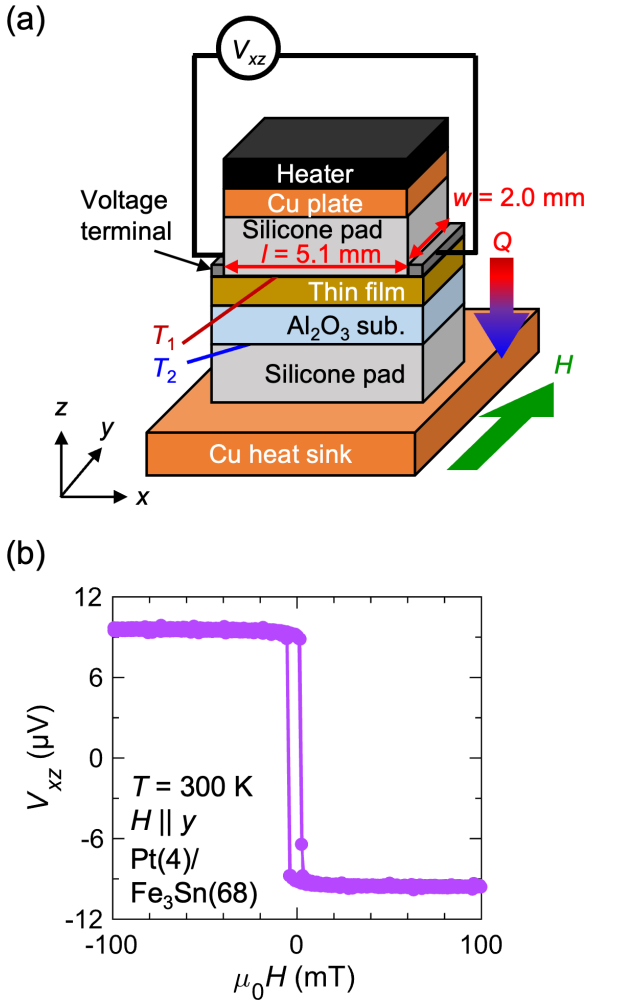

FIG. 4. (a) Schematic illustration of ANE measurement setup under the out-of-plane ∇T($||$ [0001] $||$ z) and in-plane field H($||$ [01$\bar{1}$0] $||$ y). (b) Field dependence of the Nernst voltage in the bilayer Pt/Fe_3Sn film under out-of-plane ∇T and in-plane H configuration at room temperature.

sample [39,52] (See also the Supplemental Material [57]). We confirm a clear hysteretic behavior of the Nernst voltage V_{xz} with the switching field of 20 Oe. Although ∇T is necessary to estimate ANE from V_{xz}, it is difficult to directly measure ∇T in the thickness direction of the Fe_3Sn layer. Therefore, we try to estimate ∇T using the heat flux Q and the thermal conductivity κ based on Fourier's law ($Q = \kappa\nabla T$). To obtain the heat flux flowing perpendicular to the Fe_3Sn film Q_{Fe_3Sn}, ANE of amorphous CoFeB (50 nm) films on Al_2O_3 (430 μm) substrates, which should be isotropic in character, is also measured under the same conditions as for the Fe_3Sn film (Fig. S2 in the Supplemental Material [57]). From the detailed experiments and calculations given in the Supplemental Material [57], it is estimated that a heat flux of about 0.9(2) W/cm^2 is flowing through the Fe_3Sn film in the measurement presented in Fig. 4(b). Moreover, using the thermal conductivity $\kappa_{Fe_3Sn} = 13$ W/Km of the bulk polycrystalline sample [5], the temperature gradient and the temperature difference through the Fe_3Sn layer can be estimated as $\nabla T_{Fe_3Sn} = 0.7(1)$ K/mm and $\Delta T_{Fe_3Sn} = 4.5(8) \times 10^{-5}$ K, respectively.

Therefore, we obtain ANE in the out-of-plane ∇T configuration of $V_{xz}/(l\nabla T_{Fe_3Sn}) \sim 2.9(5)\,\mu V/K$. After shunt correction, it becomes $\sim$3.6(7) μV/K, which is nearly the same value as the out-of-plane component $|S_{yx}^{calc}| = 3.0\,\mu V/K$.

Finally, the thermoelectric properties of the Fe_3Sn film are compared with those of other magnetic materials. The output voltage directly related to the sensitivity of heat flux sensors that detect perpendicular heat flux, which is considered one of the most promising applications of ANE, is shown by $V_{xz} = (S_{xz}/\kappa) \times d_{all} \times Q$, where d_{all} is the total length of the magnetic wire parallel to the direction of generated electromotive force. In other words, a material with a large S_{xz}/κ is more suitable for developing a high-sensitivity sensor. In fact, since $S_{xz}/\kappa = V_{xz}/Qd_{all}$, the coefficient of the sensor's sensitivity can be directly evaluated from the measurement shown in Fig. 4(b). In the out-of-plane ∇T configuration, V_{xz}/Qd_{all} in bilayer Pt/Fe_3Sn film is estimated to be 0.22(4) μVm/W (0.27(5) μVm/W after shunt correction). For the comparison, we estimate the coefficient of the sensor's sensitivity from S_{xz}/κ for other systems and find that the coefficient of our Fe_3Sn films is larger than one for other conventional FM materials (e.g., Py [74]: 0.02 μVm/W) and topological AFM materials (e.g., Mn_3Sn [18,75]: 0.08 μVm/W), and comparable to topological FM materials (Fe_3Al [39]; 0.22 μVm/W, Fe_3Ga [39]: 0.25 μVm/W, Co_2MnGa [38,41,76]: 0.3–0.36 μVm/W).

IV. CONCLUSION

In summary, we have succeeded in fabricating the epitaxial Fe_3Sn film with high-quality crystallinity and observed strong in-plane magnetic anisotropy comparable to the bulk single crystal. Our film shows large AHE and ANE, which are comparable to or even exceeding those reported for bulk samples. ANE under out-of-plane ∇T configuration shows the large spontaneous Nernst voltage. Our successful thin-film fabrication and findings of the large ANE lay the foundation for the thermoelectric application of the nodal plane binary system Fe_3Sn based on inexpensive elements.

ACKNOWLEDGMENTS

This work is partially supported by New Energy and Industrial Technology Development Organization (NEDO), by Japan Science and Technology Agency (JST)-MIRAI (JPMJMI20A1), JST-CREST (JPMJCR18T3), and by JST-AdCOPR (JPMJKB2306). S.K. acknowledges support from JST SPRING (JPMJSP2108). T.H. acknowledges support from the Thermal and Electric Energy Technology (TEET) Foundation and the Murata Science Foundation. Use of the facilities of the Laboratory for Magnetic and Electronic Properties at Interface and the Materials Design and Characterization Laboratory at the Institute for Solid State Physics, the University of Tokyo, is acknowledged.

[1] S. Nakatsuji, N. Kiyohara, and T. Higo, Nature (London) **527**, 212 (2015).
[2] K. Kuroda, T. Tomita, M. T. Suzuki, C. Bareille, A. A. Nugroho, P. Goswami, M. Ochi, M. Ikhlas, M. Nakayama, S. Akebi *et al.*, Nat. Mater. **16**, 1090 (2017).
[3] L. Ye, M. Kang, J. Liu, F. von Cube, C. R. Wicker, T. Suzuki, C. Jozwiak, A. Bostwick, E. Rotenberg, D. C. Bell *et al.*, Nature (London) **555**, 638 (2018).
[4] M. Kang, L. Ye, S. Fang, J.-S. You, A. Levitan, M. Han, J. I. Facio, C. Jozwiak, A. Bostwick, E. Rotenberg *et al.*, Nat. Mater. **19**, 163 (2020).
[5] T. Chen, S. Minami, A. Sakai, Y. Wang, Z. Feng, T. Nomoto, M. Hirayama, R. Ishii, T. Koretsune, R. Arita, and S. Nakatsuji, Sci. Adv. **8**, eabk1480 (2022).
[6] M. Kang, S. Fang, L. Ye, H. C. Po, J. Denlinger, C. Jozwiak, A. Bostwick, E. Rotenberg, E. Kaxiras, J. G. Checkelsky, and R. Comin, Nat. Commun. **11**, 4004 (2020).
[7] S. Cheng, M. Nrisimhamurty, T. Zhou, N. Bagués, W. Zhou, A. J. Bishop, I. Lyalin, C. Jozwiak, A. Bostwick, E. Rotenberg *et al.*, Nano Lett. **23**, 7107 (2023).
[8] D. F. Liu, A. J. Liang, E. K. Liu, Q. N. Xu, Y. W. Li, C. Chen, D. Pei, W. J. Shi, S. K. Mo, P. Dudin *et al.*, Science **365**, 1282 (2019).
[9] S. N. Guin, P. Vir, Y. Zhang, N. Kumar, S. J. Watzman, C. Fu, E. Liu, K. Manna, W. Schnelle, J. Gooth *et al.*, Adv. Mater. **31**, 1806622 (2019).
[10] R. K. Gopal Shama and Y. Singh, J. Magn. Magn. Mater. **502**, 166547 (2020).
[11] M. Kanagaraj, J. Ning, and L. He, Rev. Phys. **8**, 100072 (2022).
[12] J.-X. Yin, W. Ma, T. A. Cochran, X. Xu, S. S. Zhang, H.-J. Tien, N. Shumiya, G. Cheng, K. Jiang, B. Lian *et al.*, Nature (London) **583**, 533 (2020).
[13] W. Ma, X. Xu, J.-X. Yin, H. Yang, H. Zhou, Z.-J. Cheng, Y. Huang, Z. Qu, F. Wang, M. Z. Hasan, and S. Jia, Phys. Rev. Lett. **126**, 246602 (2021).
[14] S. Peng, Y. Han, G. Pokharel, J. Shen, Z. Li, M. Hashimoto, D. Lu, B. R. Ortiz, Y. Luo, H. Li *et al.*, Phys. Rev. Lett. **127**, 266401 (2021).
[15] H. Li, T. T. Zhang, T. Yilmaz, Y. Y. Pai, C. E. Marvinney, A. Said, Q. W. Yin, C. S. Gong, Z. J. Tu, E. Vescovo *et al.*, Phys. Rev. X **11**, 031050 (2021).
[16] Q. Wang, P. Kong, W. Shi, C. Pei, C. Wen, L. Gao, Y. Zhao, Q. Yin, Y. Wu, G. Li *et al.*, Adv. Mater. **33**, 2102813 (2021).
[17] F. H. Yu, T. Wu, Z. Y. Wang, B. Lei, W. Z. Zhuo, J. J. Ying, and X. H. Chen, Phys. Rev. B **104**, L041103 (2021).
[18] M. Ikhlas, T. Tomita, T. Koretsune, M.-T. Suzuki, D. Nishio-Hamane, R. Arita, Y. Otani, and S. Nakatsuji, Nat. Phys. **13**, 1085 (2017).
[19] T. Chen, T. Tomita, S. Minami, M. Fu, T. Koretsune, M. Kitatani, I. Muhammad, D. Nishio-Hamane, R. Ishii, F. Ishii *et al.*, Nat. Commun. **12**, 572 (2021).
[20] T. Higo, H. Man, D. B. Gopman, L. Wu, T. Koretsune, O. M. J. van 't Erve, Y. P. Kabanov, D. Rees, Y. Li, M.-T. Suzuki *et al.*, Nat. Photonics **12**, 73 (2018).
[21] T. Matsuda, N. Kanda, T. Higo, N. P. Armitage, S. Nakatsuji, and R. Matsunaga, Nat. Commun. **11**, 909 (2020).
[22] H. Tsai, T. Higo, K. Kondou, T. Nomoto, A. Sakai, A. Kobayashi, T. Nakano, K. Yakushiji, R. Arita, S. Miwa *et al.*, Nature (London) **580**, 608 (2020).

[23] T. Higo, K. Kondou, T. Nomoto, M. Shiga, S. Sakamoto, X. Chen, D. Nishio-Hamane, R. Arita, Y. Otani, S. Miwa, and S. Nakatsuji, Nature (London) **607**, 474 (2022).

[24] X. Chen, T. Higo, K. Tanaka, T. Nomoto, H. Tsai, H. Idzuchi, M. Shiga, S. Sakamoto, R. Ando, H. Kosaki *et al.*, Nature (London) **613**, 490 (2023).

[25] S. Nakatsuji and R. Arita, Annu. Rev. Condens. Matter Phys. **13**, 119 (2022).

[26] Z. Lin, J.-H. Choi, Q. Zhang, W. Qin, S. Yi, P. Wang, L. Li, Y. Wang, H. Zhang, Z. Sun *et al.*, Phys. Rev. Lett. **121**, 096401 (2018).

[27] H. Tanaka, Y. Fujisawa, K. Kuroda, R. Noguchi, S. Sakuragi, C. Bareille, B. Smith, C. Cacho, S. W. Jung, T. Muro *et al.*, Phys. Rev. B **101**, 161114 (2020).

[28] Q. Wang, Q. Yin, and H. Lei, Chin. Phys. B **29**, 017101 (2020).

[29] Q. Du, M.-G. Han, Y. Liu, W. Ren, Y. Zhu, and C. Petrovic, Adv. Quantum Technol. **3**, 2000058 (2020).

[30] Z. Lin, C. Wang, P. Wang, S. Yi, L. Li, Q. Zhang, Y. Wang, Z. Wang, H. Huang, Y. Sun *et al.*, Phys. Rev. B **102**, 155103 (2020).

[31] M. Han, H. Inoue, S. Fang, C. John, L. Ye, M. K. Chan, D. Graf, T. Suzuki, M. P. Ghimire, W. J. Cho *et al.*, Nat. Commun. **12**, 5345 (2021).

[32] Y. Satake, K. Fujiwara, J. Shiogai, T. Seki, and A. Tsukazaki, Sci. Rep. **9**, 3282 (2019).

[33] K. Fujiwara, Y. Kato, H. Abe, S. Noguchi, J. Shiogai, Y. Niwa, H. Kumigashira, Y. Motome, and A. Tsukazaki, Nat. Commun. **14**, 3399 (2023).

[34] B. C. Sales, B. Saparov, M. A. McGuire, D. J. Singh, and D. S. Parker, Sci. Rep. **4**, 7024 (2014).

[35] C. Echevarria-Bonet, N. Iglesias, J. S. Garitaonandia, D. Salazar, G. C. Hadjipanayis, and J. M. Barandiaran, J. Alloys Compd. **769**, 843 (2018).

[36] B. Fayyazi, K. P. Skokov, T. Faske, I. Opahle, M. Duerrschnabel, T. Helbig, I. Soldatov, U. Rohrmann, L. Molina-Luna, K. Güth *et al.*, Acta Mater. **180**, 126 (2019).

[37] L. Prodan, D. M. Evans, S. M. Griffin, A. Östlin, M. Altthaler, E. Lysne, I. G. Filippova, S. Shova, L. Chioncel, V. Tsurkan, and I. Kézsmárki, Appl. Phys. Lett. **123**, 021901 (2023).

[38] A. Sakai, Y. P. Mizuta, A. A. Nugroho, R. Sihombing, T. Koretsune, M.-T. Suzuki, N. Takemori, R. Ishii, D. Nishio-Hamane, R. Arita *et al.*, Nat. Phys. **14**, 1119 (2018).

[39] A. Sakai, S. Minami, T. Koretsune, T. Chen, T. Higo, Y. Wang, T. Nomoto, M. Hirayama, S. Miwa, D. Nishio-Hamane *et al.*, Nature (London) **581**, 53 (2020).

[40] M. Mizuguchi and S. Nakatsuji, Sci. Technol. Adv. Mater. **20**, 262 (2019).

[41] S. N. Guin, K. Manna, J. Noky, S. J. Watzman, C. Fu, N. Kumar, W. Schnelle, C. Shekhar, Y. Sun, J. Gooth, and C. Felser, NPG Asia Mater. **11**, 16 (2019).

[42] S. Minami, F. Ishii, M. Hirayama, T. Nomoto, T. Koretsune, and R. Arita, Phys. Rev. B **102**, 205128 (2020).

[43] C. Wuttke, F. Caglieris, S. Sykora, F. Scaravaggi, A. U. B. Wolter, K. Manna, V. Süss, C. Shekhar, C. Felser, B. BUuml;chner, and C. Hess, Phys. Rev. B **100**, 085111 (2019).

[44] F. Caglieris, C. Wuttke, S. Sykora, V. Süss, C. Shekhar, C. Felser, B. Büchner, and C. Hess, Phys. Rev. B **98**, 201107 (2018).

[45] T. Asaba, V. Ivanov, S. M. Thomas, S. Y. Savrasov, J. D. Thompson, E. D. Bauer, and F. Ronning, Sci. Adv. **7**, eabf1467 (2021).

[46] W. Zhou and Y. Sakuraba, Appl. Phys. Express **13**, 043001 (2020).

[47] H. Tanaka, T. Higo, R. Uesugi, K. Yamagata, Y. Nakanishi, H. Machinaga, and S. Nakatsuji, Adv. Mater. **35**, 2303416 (2023).

[48] A. Low, S. Ghosh, S. Ghorai, and S. Thirupathaiah, Phys. Rev. B **108**, 094404 (2023).

[49] B. P. Belbase, L. Ye, B. Karki, J. I. Facio, J.-S. You, J. G. Checkelsky, J. van den Brink, and M. P. Ghimire, Phys. Rev. B **108**, 075164 (2023).

[50] K. Fujiwara, Y. Kato, T. Seki, K. Nomura, K. Takanashi, Y. Motome, and A. Tsukazaki, Commun. Mater, **2**, 113 (2021).

[51] Y. Sakuraba, K. Hasegawa, M. Mizuguchi, T. Kubota, S. Mizukami, T. Miyazaki, and K. Takanashi, Appl. Phys. Express **6**, 033003 (2013).

[52] T. Higo, Y. Li, K. Kondou, D. Qu, M. Ikhlas, R. Uesugi, D. Nishio-Hamane, C. L. Chien, Y. Otani, and S. Nakatsuji, Adv. Funct. Mater. **31**, 2008971 (2021).

[53] T.-W. Weng, T.-C. Chuang, D. Qu, and S.-Y. Huang, J. Magn. Magn. Mater. **563**, 169892 (2022).

[54] R. F. C. Farrow, G. R. Harp, R. F. Marks, T. A. Rabedeau, M. F. Toney, D. Weller, and S. S. P. Parkin, J. Cryst. Growth **133**, 47 (1993).

[55] S. Ramanathan, B. M. Clemens, P. C. McIntyre, and U. Dahmen, Philos. Mag. A **81**, 2073 (2001).

[56] D. A. Grave, H. Dotan, Y. Levy, Y. Piekner, B. Scherrer, K. D. Malviya, and A. Rothschild, J. Mater. Chem. A **4**, 3052 (2016).

[57] See Supplemental Material at http://link.aps.org/supplemental/10.1103/PhysRevMaterials.8.054206 for the crystallographic relation between the Al_2O_3 and the Pt layer, and a detailed discussion of the evaluation of the heat flux flowing perpendicular to the film, and which includes Refs. [58–68].

[58] E. N. Maslen, V. A. Streltsov, N. R. Streltsova, N. Ishizawa, and Y. Satow, Acta Crystallogr., Sect. B: Struct. Sci. **49**, 973 (1993).

[59] L. Lutterotti and P. Scardi, J. Appl. Crystallogr. **23**, 246 (1990).

[60] J. Lewis, D. Schwarzenbach, and H. D. Flack, Acta Crystallogr., Sect. A **38**, 733 (1982).

[61] W. P. Davey, Phys. Rev. **25**, 753 (1925).

[62] E. A. Owen and E. L. Yates, The London, Edinburgh, and Dublin Philosophical Magazine and Journal of Science **15**, 472 (1933).

[63] J. W. Edwards, R. Speiser, and H. L. Johnston, J. Appl. Phys. **22**, 424 (1951).

[64] J. A. Cusidó, A. Isalgué, and J. Tejada, Phys. Status Solidi A **87**, 169 (1985).

[65] C. L. Choy, W. P. Leung, and Y. K. Ng, J. Appl. Phys. **66**, 5335 (1989).

[66] P. E. Hopkins, M. Ding, and J. Poon, J. Appl. Phys. **111**, 103533 (2012).

[67] A. Deschenes, S. Muneer, M. Akbulut, A. Gokirmak, and H. Silva, Beilstein J. Nanotechnol. **7**, 1676 (2016).

[68] Y. Ma, W. Yang, J. Pei, H. Li, H. Lu, H. Liu, M. Li, W. Li, X. Sun, J. Li, and A. Inoue, J. Non-Cryst. Solids **576**, 121264 (2022).

[69] W. J. Xu, B. Zhang, Z. Wang, S. S. Chu, W. Li, Z. B. Wu, R. H. Yu, and X. X. Zhang, Eur. Phys. J. B **65**, 233 (2008).
[70] X. Kou, J.-M. Schmalhorst, V. Keskin, and G. Reiss, J. Appl. Phys. **112**, 093915 (2012).
[71] D. Xiao, Y. Yao, Z. Fang, and Q. Niu, Phys. Rev. Lett. **97**, 026603 (2006).
[72] D. Xiao, M.-C. Chang, and Q. Niu, Rev. Mod. Phys. **82**, 1959 (2010).
[73] G. Sharma, P. Goswami, and S. Tewari, Phys. Rev. B **93**, 035116 (2016).
[74] D. Khadka, T. R. Thapaliya, S. Hurtado Parra, J. Wen, R. Need, J. M. Kikkawa, and S. X. Huang, Phys. Rev. Mater. **4**, 084203 (2020).
[75] X. Li, L. Xu, L. Ding, J. Wang, M. Shen, X. Lu, Z. Zhu, and K. Behnia, Phys. Rev. Lett. **119**, 056601 (2017).
[76] L. Xu, X. Li, L. Ding, T. Chen, A. Sakai, B. Fauqué, S. Nakatsuji, Z. Zhu, and K. Behnia, Phys. Rev. B **101**, 180404 (2020).
[77] K. Momma and F. Izumi, J. Appl. Crystallogr. **44**, 1272 (2011).